*J. Min. Metall. Sect. B-Metall. 61 (3) (2025) 399 - 409*

**Journal of Mining and Metallurgy, Section B: Metallurgy**

# DISSOLUTION KINETIC MECHANISMS OF $FeCr_2O_4$ SPINEL IN MgO-$Al_2O_3$-$SiO_2$ SLAG SYSTEM: ELEMENTAL DISSOLUTION AND COMPONENT DIFFUSION

**Kang Shao [a], Zhang Chen [a], Lijun Wang [a, b, *]**

[a] University of Science and Technology Beijing,Collaborative Innovation Center of Steel Technology, Beijing, China

[b] University of Science and Technology Beijing,State Key Laboratory of Advanced Metallurgy, Beijing, China

*(Received 11 July 2025; Accepted 21 December 2025)*

***Abstract***

*The molten chromite reduction direct alloying process serves as a pivotal metallurgical technology in stainless steel production, offering advantages such as reduced carbon consumption and improved production efficiency. In this study, to reveal the dissolution mechanism of chromite, pure phase of synthetic $FeCr_2O_4$, the main component of chromite, was used to replace chromite with complex compositions. The dissolution kinetics of $FeCr_2O_4$ in MgO-$Al_2O_3$-$SiO_2$ slag were systematically investigated as functions of stirring intensity, MgO/$SiO_2$, and temperature, revealing its non-isothermal reactive dissolution characteristics. Experimental results demonstrated that the solubility of $Cr_2O_3$ exhibited a trend of initial increase followed by subsequent decrease as the MgO/$SiO_2$ mass ratio increased. The maximum solubility was observed at a MgO/$SiO_2$ mass ratio of 0.56. Additionally, temperature-related studies indicated that the dissolution of $FeCr_2O_4$ is progressively enhanced with increasing temperature under elevated thermal conditions (1500-1600 ℃). Meanwhile, scanning electron microscopy (SEM) analyses confirmed that the interfacial reaction between $FeCr_2O_4$ and slag components generated $MgAl_2O_4$, $MgCr_2O_4$ and MgO-xFeO solid solution, forming a boundary layer on the surface of unreacted $FeCr_2O_4$.The dissolution reaction on the surface of $FeCr_2O_4$ was the rate-controlling step in the dissolution process. The calculated activation energy of the dissolution process was 65.43 kJ·mol$^{-1}$.*

***Keywords***: *Slag; Dissolution; MgO/ $SiO_2$; Interface; Dissolution kinetics*

## 1. Introduction

Chromium, as a critical alloying element in steelmaking, plays an irreplaceable role in stainless steel production. However, industrial utilization of chromite resources faces significant technical challenges since current industrial practices predominantly employ submerged arc furnace (SAF) smelting for ferrochrome (FeCr) production as chromium source [1].

As a crucial raw material for producing stainless steel, acid-resistant steel, and heat-resistant steel, the market demand for ferrochrome continues to grow. China's stainless steel output reached 35 million tons in 2022, accounting for approximately 60% of global production [2, 3]. Statistical analyses indicate that each ton of stainless steel requires 300-400 kg of ferrochrome [4]. Notably, China's chromite ore imports reached 14.96 million tons in 2022, with over 80% sourced from South Africa, creating supply chain vulnerabilities due to highly concentrated import sources. This conventional method exhibits notable environmental and economic limitations, characterized by ultra-high energy consumption (averaging 3-5 times higher than blast furnace ironmaking processes, approximately 2150 kgce/t) and substantial CO/$CO_2$ gas emissions contributing to atmospheric pollution and environmental degradation [2-6]. The substantial energy demand primarily originates from the high reduction temperature of $Cr_2O_3$ and the high melting point characteristics of chromium-containing melts [7, 8]. Consequently, improving chromite utilization efficiency and reducing carbon emission intensity have become urgent industrial and technical challenges [9]. The development of cost-effective chromite processing technologies could not only enhance resource efficiency but also mitigate environmental impacts [10-15].

*Corresponding author: lijunwang@ustb.edu.cn*

***https://doi.org/10.2298/JMMB250711031S***

The composition of slag is closely related to the dissolution and reduction of chromite. O. Demir et al. [16] investigated chromite smelting reduction in CaO-MgO-$Al_2O_3$-$SiO_2$ quaternary slag systems, identifying concurrent dissolution and reduction stages during the process, with dissolution predominating during initial stages. However, the refractory nature of chromite's gangue constituents (e.g., $FeCr_2O_4$, MgO, $Al_2O_3$) necessitates fluxing agents to convert insoluble components into molten slag, thereby enhancing chromium reducibility. Subsequent studies [17, 18] revealed that $SiO_2$ addition promotes the formation of low-melting-point compounds and reactive slags, significantly improving reduction efficiency. Z. Wang et al. [19] demonstrated that chromium content in CaO-$SiO_2$-MgO-$Al_2O_3$-$Cr_2O_3$ stainless steel slags decreased progressively as the $Al_2O_3/SiO_2$ mass ratio increased from 0.125 to 0.5. In contrast, Y. Liu et al. [20, 21] established an inverse correlation between chromite dissolution and slag basicity (B=0.8-1.6), while elevated $Al_2O_3$ and MgO concentrations exhibited inhibitory effects. Complementing these findings, Morita et al. [22] quantified $MgO{\cdot}Cr_2O_3$ solubility in MgO-$SiO_2$-$Al_2O_3$-CaO slags at 1600 °C under ambient conditions, observing a negative correlation with $Al_2O_3$ and MgO mass% that aligns with chromite dissolution suppression mechanisms. H. Katayama et al. [23] systematically investigated chromite reduction in CaO-$SiO_2$-MgO-$Al_2O_3$ slag systems (1550-1650 °C) through powder mixing with graphite, revealing surface-initiated reduction followed by slag-component infiltration that enhanced internal dissolution. Furthermore, D. Yu et al. [24] employed thermogravimetric analysis coupled with off-gas monitoring to characterize carbothermic reduction under nickel catalysis. Their results demonstrated that the process followed a multi-stage mechanism, with progressive formation of refractory oxide layers on chromite surfaces causing a kinetic transition from chemical reaction control to diffusion limitation. Notably, nickel addition demonstrated marked promotional effects on chromite reduction at temperatures exceeding 1300 °C, primarily attributed to the formation of low-melting-point alloys.

The basicity of slag and additives also exhibit distinct effects on the dissolution and reduction of chromite ore. D. Paktunc et al. [25] established through chromite smelting reduction experiments that elevated slag basicity effectively decreases the chromium slag-metal distribution ratio while enhancing chromium metallization. T. Takaoka et al. [26] systematically evaluated direct reduction behaviors in converter furnaces using slags containing 30 wt% $B_2O_3$ and 30 wt% $CaF_2$ respectively, demonstrating substantial acceleration in reduction kinetics. However, $CaF_2$-containing slags induced severe corrosive effects on furnace refractory linings, necessitating due consideration to operational longevity in practical applications.

Current research on chromite smelting reduction predominantly focuses on reduction processes, while systematic investigation of dissolution behavior, particularly dissolution mechanisms under non-reducing conditions, remains notably underexplored. Furthermore, the complex compositional matrix of natural chromite ores introduces significant complexities that fundamentally alter slag system characteristics, thereby complicating mechanistic interpretation. This study employed synthetic iron-chromium spinel ($FeCr_2O_4$) as a model material under an inert atmosphere to systematically examine the dissolution kinetics influenced by agitation intensity, $MgO/SiO_2$ mass ratio, and temperature (1550-1650 °C). By studying the element distribution on the ore/slag interface, we have conclusively identified the rate-limiting steps at spinel-slag interfaces, ultimately establishing a comprehensive dissolution kinetic model incorporating both boundary layer diffusion and interfacial reaction mechanisms.

## 2. Experiment

### *2.1. Materials*

All chemical reagents used in this study were of analytical grade. $FeCr_2O_4$ was synthesized via a high-temperature solid-state synthesis method. Specifically, Fe, $Cr_2O_3$, $Fe_2O_3$, $SiO_2$, MgO, and $Al_2O_3$were purchased from Sinopharm Chemical Reagent Co., Ltd. High-purity argon gas (Ar, 99.999% purity) for maintaining an inert atmosphere during experiments was supplied by Praxair Inc. (Beijing Branch).

The reaction equation for the synthesis of $FeCr_2O_4$ via the solid-state reaction method can be represented by Equation (1):

$$Fe + Fe_2O_3 + 3Cr_2O_3 = 3FeCr_2O_4 \quad (1)$$

The precursor mixture was formulated with a stoichiometric ratio of Fe:$Fe_2O_3$:$Cr_2O_3$ = 1:1:3. Initially, chromium oxide ($Cr_2O_3$) and iron oxide ($Fe_2O_3$) were homogeneously mixed according to the stoichiometric ratio, followed by 20-hour ball milling in ethanol using zirconia grinding media. The resulting slurry was dried in an oven at 110 °C for 12 hours to obtain mixed oxide powders. Subsequently, stoichiometrically calculated iron powder (Fe, 200 mesh) was added and further blended in an agate mortar for 30 min to ensure homogeneity. The final mixture was loaded into a pure iron crucible with a

lid, which was then placed inside a graphite crucible (70 mm diameter × 150 mm height). This dual-crucible configuration ensured a continuous reducing atmosphere during synthesis. The graphite crucible assembly was loaded into a silicon-molybdenum resistance furnace and calcined at 1373 K for 24 h under continuous argon flow (100 mL/min). The calcined product was crushed into fine particles for XRD characterization. As shown in Figure 1, the three strongest diffraction peaks of the obtained XRD pattern matched well with the reference $FeCr_2O_4$ phase (PDF#98-000-0161, JADE 9 database), confirming the formation of pure phase $FeCr_2O_4$. The synthesized powder was then pulverized and sieved through an 80-mesh sieve. Finally, the mixed powder was pressed into a cylindrical under a pressure of 20 MPa with dimensions of Ø15 mm × 15 mm height. These pressed cylinders were then sintered at 1673 K for 4 h under an argon atmosphere (flow rate: 1 L/min) to achieve the required mechanical strength for subsequent experiments. The dissolution behavior of $FeCr_2O_4$ in molten slag was investigated using a $MgO$-$Al_2O_3$-$SiO_2$ ternary slag system, with experimental parameters detailed in Table 1. Complementary thermodynamic calculations were performed using FactSage 8.3 to predict the liquidus temperatures of different slag compositions, as summarized in Table 2.

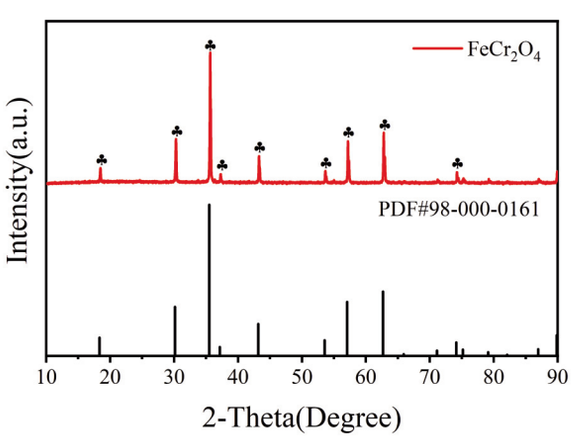


***Figure 1.*** *XRD pattern of synthesized $FeCr_2O_4$*

***Table 1.*** *Experimental scheme*

| | w(MgO) | w($SiO_2$) | w($Al_2O_3$) | MgO/$SiO_2$ | Experimental temperature(℃) |
|---|---|---|---|---|---|
| Slag1 | 37.93 | 37.93 | 24.14 | 1 | 1600 |
| Slag 2 | 27.28 | 48.58 | 24.14 | 0.56 | 1600 |
| Slag 3 | 18.82 | 57.04 | 24.14 | 0.33 | 1600 |
| Slag 4 | 36 | 64 | | 0.56 | 1600 |
| Slag 5 | 27.28 | 48.58 | 24.14 | 0.56 | 1550 |
| Slag 6 | 27.28 | 48.58 | 24.14 | 0.56 | 1500 |

### *2.2. Apparatus Procedure*

All experiments were conducted in a vertical $MoSi_2$-element resistance furnace. A 100 g slag sample was loaded into a molybdenum crucible (60 mm × 70 mm), which was then positioned in the furnace chamber. The system was heated to the target temperature of 1600 °C via program-controlled heating under an argon atmosphere (flow rate: 1 L/min) to prevent oxidation of the crucible. After reaching thermal equilibrium, the slag was homogenized by holding at the target temperature for 1 h, followed by initial slag sampling. The $FeCr_2O_4$ cylindrical specimen was then immersed into the molten slag. Slag samples were collected at 15, 30, 45, 60, and 90 min intervals and immediately water-quenched, with consistent sampling positions maintained throughout. During the dissolution experiment, the rotational speed of the molybdenum stirrer was maintained at 150 rpm unless otherwise specified in comparative studies. Upon reaction completion, the crucible was immediately subjected to water quenching.

The solubility was determined by measuring elemental concentrations in slag samples collected at predetermined time intervals. Inductively coupled plasma optical emission spectrometry (ICP-OES) was employed for chemical analysis. (Optima7000DV, PerkinElmer, America).

The microstructural morphology of the dissolution products was examined using scanning electron microscopy (SEM, FEI Quanta, Netherlands), and line-scan energy-dispersive spectroscopy (EDS) analysis was conducted to characterize the compositional profile across the dissolution interface.

## 3. Results and Discussions

### *3.1. The effects of stirring on the dissolution behavior of $FeCr_2O_4$*

Figure 2 illustrates the dissolution behavior of pure phase $FeCr_2O_4$ in slag under conditions of 1600 °C and MgO/$SiO_2$=0.56. The data demonstrate significant variations in $Cr_2O_3$ solubility within the molten slag

under different stirring conditions. At the maximum dissolution time of 90 min, a maximum solubility of 0.143% was achieved under stirred slag conditions, compared to 0.081% under static conditions. Notably, the solubility disparity between stirred and non-stirred systems progressively widened with time. At 60 min of dissolution, the $Cr_2O_3$ solubility under stirring was 1.77 times higher than that in the static system. This phenomenon originates from the forced convection induced by stirring, which significantly enhances the flow velocity of molten slag around spinel particles during dissolution. According to Fick's first law of diffusion, the diffusion flux is proportional to the concentration gradient. Stirring stabilizes the concentration gradient between the spinel surface and bulk slag, thereby accelerating mass transfer during dissolution and promoting rapid diffusion of ionic into the slag matrix. In contrast, static conditions allow the formation of a stagnant diffusion boundary layer at the spinel-slag interface, which impedes particle transport. Stirring to a certain extent can destroy this diffusion layer, so that its thickness is reduced, providing more favourable mass transfer conditions for the dissolution of spinel. Continuous slag flow renews reaction interfaces, enabling fresh slag to contact reactants while efficiently removing reaction products.

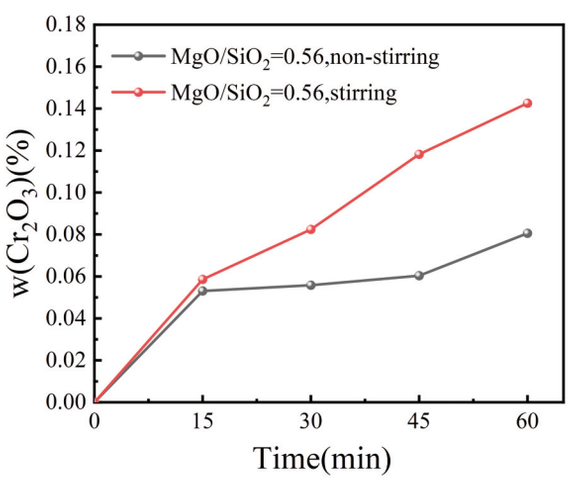


***Figure 2.*** *Effect of stirring conditions on the dissolution of $FeCr_2O_4$*

### *3.2. Effect of $MgO/SiO_2$ on the dissolution behavior of $FeCr_2O_4$*

Figure 3 delineates the influence of the $MgO/SiO_2$ mass ratio on the solubility of synthetic $FeCr_2O_4$. The dissolved $Cr_2O_3$ content in the slag exhibited a non-monotonic dependence on the $MgO/SiO_2$ mass ratio. With the decrease of $w(MgO)/w(SiO_2)$ ratio, the content of $Cr_2O_3$ dissolved into the slag showed a tendency of increasing and then decreasing, $w(MgO)/w(SiO_2)$=1 to $w(MgO)/w(SiO_2)$=0.56, $w(Cr_2O_3)$ increased from 0.012% to 0.143% at 90 min, a 11-fold increase. Therefore, the decrease of $MgO\text{-}SiO_2$ mass ratio contributed to the dissolution of $FeCr_2O_4$, but the continual decrease of $MgO\text{-}SiO_2$ mass ratio up to 0.33 would inhibit the dissolution of the dissolution of $FeCr_2O_4$ was inhibited when the Mg-Si mass ratio was lowered to 0.33.

As shown in Table 2, the $MgO/SiO_2$ mass ratio exhibited an inverse correlation with slag viscosity (η). When the slag magnesium-silicon mass ratio decreases, the slag viscosity shows a rising trend, and the liquidity of the slag will be decreased to some extent. $w(MgO)/w(SiO_2)$=0.33, the viscosity of the slag increases greatly, which is significantly higher than that of the slag when $w(MgO)/w(SiO_2)$=1, but from the figure, it can be seen that the amount of dissolution of $Cr_2O_3$ in the magnesium-silicon mass ratio is 0.33, is greater than that of $Cr_2O_3$ dissolution in magnesium-silicon mass ratio is 1, which indicates that viscosity is not the main factor that affects the dissolution of $FeCr_2O_4$. greater than the dissolved amount of $Cr_2O_3$ when the Mg-Si mass ratio is 1, which indicates that the viscosity is not the main factor affecting the dissolution of $FeCr_2O_4$. And the $MgO/SiO_2$ in the slag system is the main influencing factor.

***Table 2.*** *Theoretical melting points and viscosities of different $w(MgO)/w(SiO_2)$ slags*

| | $w(MgO)/w(SiO_2)$ | Theoretical melting point | viscosity (Pa·s) |
|---|---|---|---|
| Slag1 | 1 | 1380.6 | 0.217 |
| Slag 2 | 0.56 | 1380.6 | 0.724 |
| Slag 3 | 0.33 | 1360.3 | 3.04 |

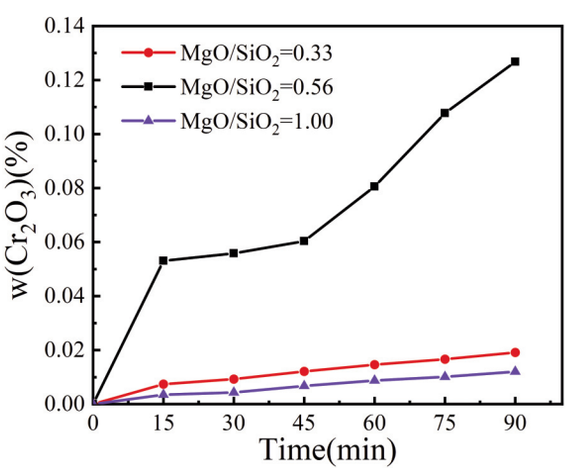


***Figure 3.*** *Effect of $w(MgO)/w(SiO_2)$ on the dissolution of $FeCr_2O_4$ (T=1600°C)*

### 3.3. Effect of temperature on the dissolution of $FeCr_2O_4$

The temperature dependence of $FeCr_2O_4$ solubility was systematically investigated using Slag 2 within the 1500-1600 °C range. From Fig. 4, it can be seen that the dissolution rate of $FeCr_2O_4$ is faster at 0-75 min, and the dissolution reaction gradually slows down after 75 min, and the solubility tends to stabilise. With the gradual increase of temperature, the solubility of $Cr_2O_3$ at each time point is increased. The maximum w($Cr_2O_3$) was 0.1127% at T=1600 °C and reaction time of 90 min, while the maximum w($Cr_2O_3$) was 0.1% and 0.08% at temperatures of 1550 °C and 1500 °C, respectively. With the increase of temperature, the overall increasing trend of solubility was not obvious before 75 min, and after 75 min, the solubility of $Cr_2O_3$ was enhanced to some extent with the increase of temperature.

The enhanced solubility of $FeCr_2O_4$ at elevated temperatures is primarily attributed to the following factors: The dissolution of $FeCr_2O_4$ into slag is an endothermic process, where increased temperature thermodynamically favors the forward reaction. Elevated temperature intensifies ionic thermal motion, increasing average kinetic energy, thereby reducing the energy barrier for Fe/Cr ions to escape lattice constraints and diffuse into the slag. Temperature-dependent slag viscosity reduction elevates ion diffusion coefficients, accelerating mass transfer during dissolution.

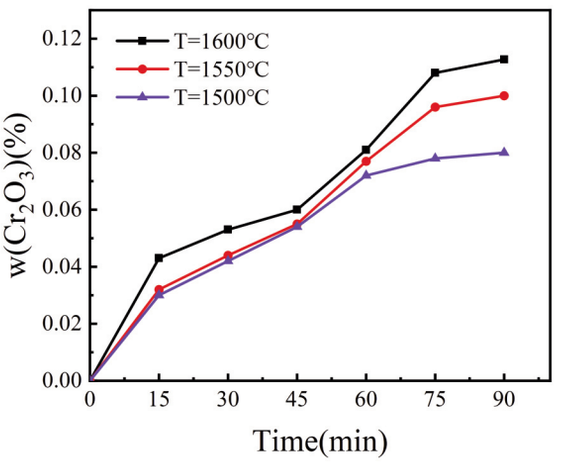


***Figure 4.*** *Effect of temperature on the dissolution of $FeCr_2O_4$*

### 3.4. Elemental distribution at the slag/$FeCr_2O_4$ interface

The analysis of elemental distribution at the slag/$FeCr_2O_4$ interface and diffusion characteristics of different elements during dissolution revealed the rate-limiting factors in $FeCr_2O_4$ dissolution.

Figure 5 illustrates the slag/$FeCr_2O_4$ interfacial evolution in Slag 2 at distinct dissolution stages (15 min, 45 min, 60 min, and 90 min). A well-defined interface and transitional layer are observable at the $FeCr_2O_4$-slag contact zone. In the scanning electron

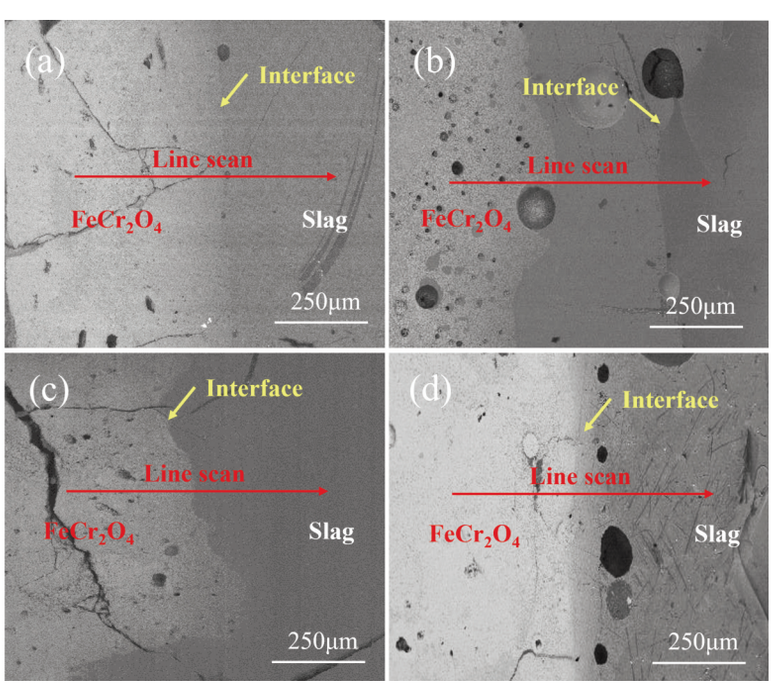


***Figure 5.*** *SEM images of the slag/$FeCr_2O_4$ interface ((a) 15 min; (b) 45 min; (c) 60 min; and (d) 90 min)*

microscopy (SEM) images, the light-contrast regions correspond to the $FeCr_2O_4$ phase, while the dark-contrast areas represent the slag phase. Contrast evolution at the slag/$FeCr_2O_4$ interfacial boundary reveals time-dependent phase interactions. The diminishing chromatic disparity over dissolution duration indicates the progressive development of a boundary layer on the $FeCr_2O_4$ side proximal to the slag phase. Meanwhile, As revealed by the elemental distributions in Figure 6 and Table 3, MgO exhibits progressive penetration into $FeCr_2O_4$ with increasing distance from the boundary layer, contrasting with the limited mobility of $SiO_2$ and $Al_2O_3$. This differential behavior confirms enhanced interfacial diffusivity of MgO and its stronger binding affinity with FeO and $Cr_2O_3$.It can be inferred that the $MgCr_2O_4$-$MgAl_2O_4$-$Mg_{1-x}Fe_xO$ mixed solid solution layer functions as a kinetic barrier isolating $FeCr_2O_4$ from molten slag contact.

The elemental gradient EDS line scanning analysis in Figure 7 quantitatively confirmed the formation of a distinct interfacial boundary layer between $FeCr_2O_4$ and the slag phase, which exhibited time-dependent thickening behavior. Temporal evolution analysis demonstrates progressive boundary layer thickening, reaching 220 μm, 240 μm, and 279.43 μm at 45 min, 60 min, and 90 min, respectively, and the growth rate of the boundary layer is basically stable at about 1.3 μm/min thereafter. It can be observed from the boundary layer that the elements Mg, Al, and Si exhibit gradient variations in sequence from. The contents of Mg, Al, and Si progressively increase from $FeCr_2O_4$ through the boundary to the slag phase, while the concentrations of Fe and Cr demonstrate a gradual decrease in the boundary layer with increasing distance from $FeCr_2O_4$.

Figure 8 illustrates the standard Gibbs free energies of several potential spinel phases formed in the system under the experimental temperature conditions. Among these spinel phases, $MgCr_2O_4$ exhibits the highest thermodynamic stability at the investigated temperatures. Based on thermodynamic principles, it can be reasonably inferred that the formed spinel solid solution predominantly consists of $MgCr_2O_4$, with minor amounts of $MgAl_2O_4$ incorporated.

Furthermore, previous investigations [27-30] have demonstrated that during high-temperature solid-liquid reactions, FeO and MgO interact to form $Mg_{1-x}Fe_xO$ solid solutions, which subsequently dissolve into the molten slag. This phenomenon effectively accounts for the observed concentration gradients of Mg, Al, and Fe within the boundary layer.

As the reaction proceeds, the thickness of the boundary layer exhibits a steady increase over time. Meanwhile, the dissolution rate of $FeCr_2O_4$ gradually slowed down. As evident from the elemental distributions in Fig. 6 and Table 3, MgO exhibits higher diffusivity compared to $SiO_2$ and $Al_2O_3$, along with stronger bonding affinity with FeO and $Cr_2O_3$ as the distance from the boundary layer increases. This facilitates the preferential formation of refractory spinel phases in the boundary layer, thereby impeding the dissolution of $FeCr_2O_4$.It can be inferred that the mixed solid solution boundary layer composed of $MgCr_2O_4$, $MgAl_2O_4$, and $Mg_{1-x}Fe_xO$ solid solution acted as a physical barrier to prevent the direct contact between $FeCr_2O_4$ and the slag. This obstruction significantly inhibited the dissolution reaction. Eventually, the termination of the dissolution reaction was mainly attributed to the continuous thickening of the mixed solid solution boundary layer.

***Table 3.*** *Slag2, EDS analysis of samples with a reduction time of 90 min (wt%)*

| | MgO | $SiO_2$ | $Al_2O_3$ | FeO | $Cr_2O_3$ |
|---|---|---|---|---|---|
| 1 | 7.42 | | | 26.94 | 65.64 |
| 2 | 9.65 | 2.32 | 5.94 | 22.73 | 59.36 |
| 3 | 9.62 | 23.16 | 13.56 | 19.5 | 34.18 |

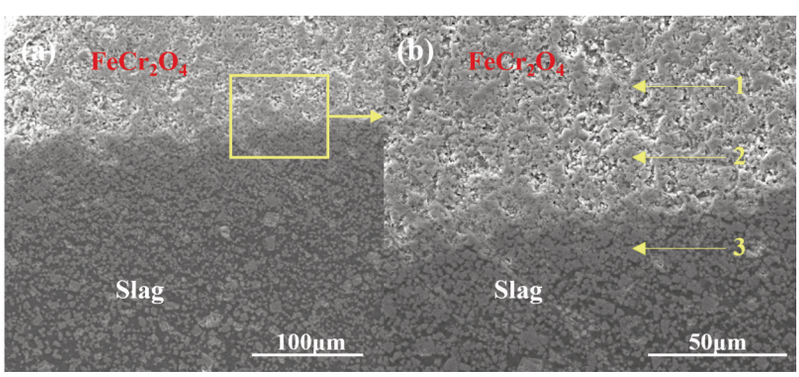


***Figure 6.*** *Elemental content distribution profile at the $FeCr_2O_4$/slag interface (Slag2, 90 min)*

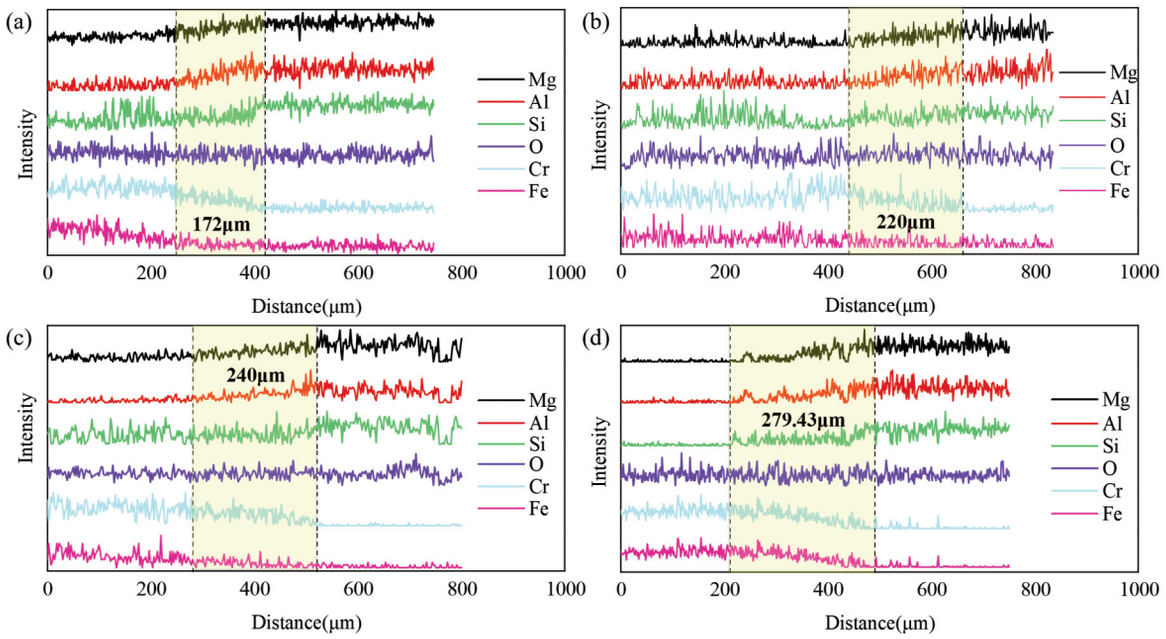


***Figure 7.*** *Elemental distribution at the slag/$FeCr_2O_4$ interface ((a) 15 min; (b) 45 min; (c) 60 min and (d) 90 min after the start of the reaction)*

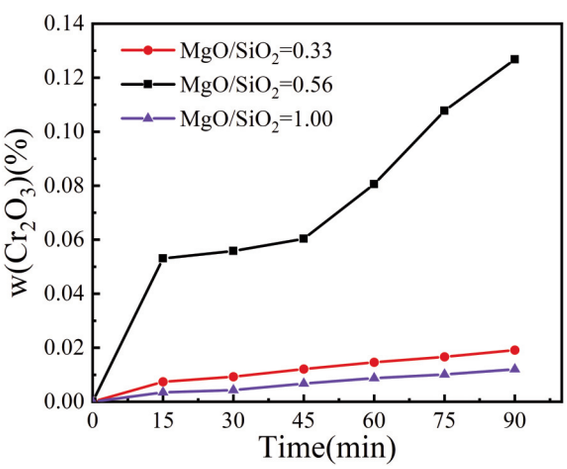


***Figure 8.*** *Standard Gibbs free energy for partial spinel generation*

### *3.5. Kinetic modelling of $FeCr_2O_4$ dissolution in slag*

The synthetic $FeCr_2O_4$ used in this experiment was substituted for chromite, and the dissolution reaction can be expressed as equation (2):

$$FeCr_2O_4 = (FeO) + (Cr_2O_3) \tag{2}$$

The dissolution process can be divided into two distinct stages: (1) the dissolution reaction of $FeCr_2O_4$ at the interface, and (2) the diffusion of liquid products from the reacted $FeCr_2O_4$ surface into the molten slag. Therefore, the unreacted nucleus model can be effectively applied to describe the macroscopic kinetics of the dissolution process.

Interfacial elemental distribution and thermodynamic analyses reveal a continuous depletion of chromium content within the boundary layer, accompanied by an abrupt change at the slag phase/boundary layer interface where chromium concentration exhibits a significant reduction. The dissolution mechanism can be elucidated as follows: Initial surface dissolution of $FeCr_2O_4$ releases FeO and $Cr_2O_3$, which subsequently diffuse outward through the boundary layer. During the migration process, these components interact with MgO and $Al_2O_3$ in the slag phase, leading to the formation of $(Mg,Fe)(Al,Cr)_2O_4$-type spinel solid solutions. Meanwhile, the redissolution of these metastable phases within the molten slag facilitates the reincorporation of FeO and $Cr_2O_3$ into the slag matrix. This dissolution-recrystallization cyclic process establishes characteristic concentration gradients of Fe and Cr, demonstrating progressive attenuation in elemental content with proximity to the slag phase. It is noteworthy that the mixed solid solution layer exhibits time-dependent growth kinetics, demonstrating a thickness increase from 172 μm to 279.43 μm within 75 min. This ultimately establishes a diffusion barrier that physically isolates the unreacted core from the slag phase. The reaction process can be formally described by Equation (3):

$$(Mg,Fe)O\cdot(Cr,Al,Fe)_2O_3 \rightarrow \left[(MgO),(FeO)\right] + \left[(Cr_2O_3),(Al_2O_3),(Fe_2O_3)\right] \tag{3}$$

According to Fick's first law, the mass transfer rate of $FeCr_2O_4$ to the slag through the slag/$FeCr_2O_4$ interface is:

$$V_b = k_b\left(C^{in}_{Cr_2O_3} - C^{S}_{Cr_2O_3}\right) \tag{4}$$

In the equation, $k_b$ represents the mass transfer rate coefficient of $Cr_2O_3$ ($mol\cdot m^{-2}\cdot s^{-1}$); $C^{in}_{Cr_2O_3}$ and $C^{S}_{Cr_2O_3}$ are the molar concentrations of $Cr_2O_3$ at the slag/$FeCr_2O_4$ interface and within the bulk slag phase, respectively ($mol\cdot cm^{-3}$).

The dissolution reaction can be considered a first-order irreversible process during the dissolution stage. Consequently, the interfacial dissolution kinetics of $FeCr_2O_4$ can be mathematically expressed by Equation (5):

$$V_r = k_r f(C^{in}_{Cr_2O_3}) \tag{5}$$

In the equation, $k_r$ represents the chemical reaction rate constant($s^{-1}$); $f(C^{in}_{Cr_2O_3})$ denotes a functional dependence on $(C^{in}_{Cr_2O_3})$, where the function is explicitly defined as $f(C^{in}_{Cr_2O_3}) = (C^{in}_{Cr_2O_3})$.

The entire dissolution process operates under quasi-steady-state conditions. Consequently, it can be postulated that the dissolution kinetics of $FeCr_2O_4$ equals the mass transfer rate of liquid-phase products at the interface throughout the process,i.e., $V_b=V_r=V$. By simultaneously solving Equations (4) and (5), Equation (6) is derived:

$$v = \frac{A\cdot C^{S}_{Cr_2O_3}}{\frac{1}{k_r}-\frac{1}{k_b}} \tag{6}$$

By defining $\frac{1}{k_r}-\frac{1}{k_b}=\frac{1}{k}$, in Equation (6), where k represents the overall resistance during the dissolution reaction process; A denotes the interfacial contact area between the slag phase and $FeCr_2O_4$($cm^2$),Equation (6) can thus be simplified to Equation (7):

$$v = kAC^{S}_{Cr_2O_3} \tag{7}$$

The consumption rate of $FeCr_2O_4$ during the dissolution process can be quantified as its volumetric reduction rate per unit time, as expressed in Equation (8):

$$R_s = -\frac{\rho dV}{Mdt} \tag{8}$$

In the equation: ρ denotes the density of $FeCr_2O_4$ (The density of $FeCr_2O_4$ was measured to be 2.8 $g\cdot cm^{-3}$ using the drainage method.); V is the volume of $FeCr_2O_4$, $cm^{-3}$; M is the molar mass of $FeCr_2O_4$, $g\cdot mol^{-3}$. The stoichiometric number gives M as 223.85 $g\cdot mol^{-3}$; t is the reaction time.

The rate of consumption of $FeCr_2O_4$ is equal to the total rate during the dissolution reaction, so $v=R_S$:

$$kAC^{S}_{Cr_2O_3} = -\frac{\rho dV}{Mdt} \tag{9}$$

Because the mass transfer process is very fast, the resistance in the mass transfer process is negligible. Therefore, the dissolution reaction on the surface of $FeCr_2O_4$ can be considered as the controlling step of the whole dissolution process. So, $k\approx k_r$ ,the reaction can be expressed as equation (10):

$$k_rAC^{S}_{Cr_2O_3} = -\frac{\rho dV}{Mdt} \tag{10}$$

The morphology of $FeCr_2O_4$ exhibits a cylindrical configuration. The dissolution model for the cylindrical solid immersed in liquid can be simplified as radial contraction of the solid phase. By substituting the corresponding volume and surface area parameters, the mathematical representation is formulated as shown in Equation (11):

$$2\pi rr + hk_rC^{S}_{Cr_2O_3} = -\frac{\rho}{M}\cdot 2\pi rh\cdot\frac{dr}{dt} \tag{11}$$

The integrated form of the simplified equation is obtained by performing integration on both sides, yielding the expression presented in Equation (12):

$$t_i = \frac{\rho h}{Mk_rC^{S}_{Cr_2O_3}}\ln\left(\frac{r_0+h}{r_i+h}\right) \tag{12}$$

The system parameters are defined as follows: $r_o$ and $r_i$ represent the initial radius of $FeCr_2O_4$ and its radius at reaction time $t_i$; respectively, while h denotes the height of $FeCr_2O_4$. Substituting the experimental data into the equation yields the relationship between time t and $\ln(\frac{r_0+h}{r_i+h})/C^{S}_{Cr_2O_3}$ . As illustrated in Figure 9, a linear correlation is observed between t and $\ln(\frac{r_0+h}{r_i+h})/C^{S}_{Cr_2O_3}$ .

The apparent rate constant kr can be determined from the slope of the linear relationship between t and $\ln(\frac{r_0+h}{r_i+h})/C^{S}_{Cr_2O_3}$ . The temperature dependence of kr obeys the Arrhenius law, as expressed by Equation (13):

$$k_r = Ae^{-\frac{E}{RT}} \tag{13}$$

The relationship between $\ln k_r$ and 1/T is plotted in Figure 10, revealing a linear correlation between $k_r$ and

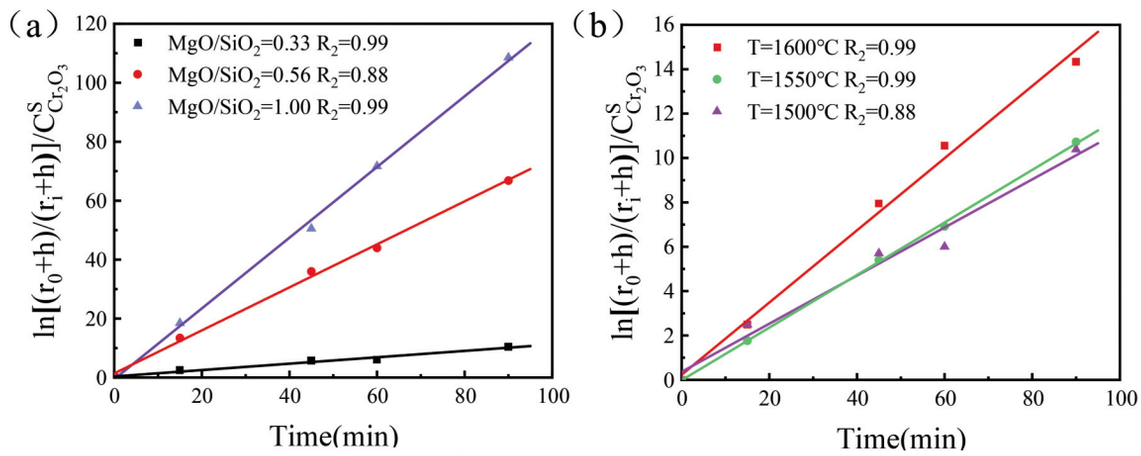


***Figure 9.*** *The correlation between t and* $\ln(\frac{r_0+h}{r_i+h}) / C^S_{Cr_2O_3}$ *is graphically represented in: (a) different MgO/SiO₂, (b) different temperatures*

temperature. This linear behavior enables the determination of the activation energy (E=65.43 kJ·mol$^{-1}$) for the dissolution reaction. In contrast, Liu et al reported a significantly higher activation energy (524.34 kJ·mol$^{-1}$) for chromite dissolution. The markedly lower activation energy demonstrates that pure $FeCr_2O_4$ dissolution requires less energy than chromite dissolution, indicating that the rate-controlling step occurs at the interfacial dissolution reaction.

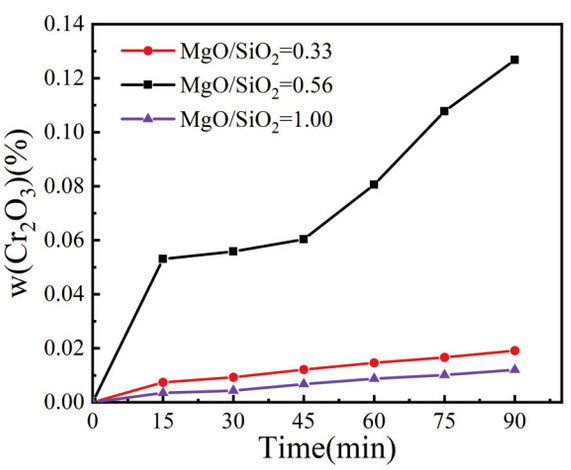


***Figure 10.*** *The relationship between lnkr and 1/T is plotted*

## 4. Conclusions

This study systematically investigates the dissolution behavior of synthetic $FeCr_2O_4$ in the $MgO\text{-}Al_2O_3\text{-}SiO_2$ slag system, with particular focus on the effects of stirring conditions, MgO/ $SiO_2$ mass ratio, and temperature. A dissolution kinetic model was established, and the principal conclusions are summarized as follows:

(1) The dissolution behavior of $Cr_2O_3$ in molten slag exhibited significant variations under different stirring conditions. Under stirred conditions, the maximum solubility reached 0.143 wt%, whereas only 0.081 wt% was observed without stirring. When the MgO/ $SiO_2$ mass ratio decreased from 1 to 0.56 under stirring conditions, the solubility of $FeCr_2O_4$ increased proportionally. Conversely, further reduction of the ratio from 0.56 to 0.33 resulted in decreased solubility. These findings demonstrate that the optimal dissolution parameters correspond to a MgO/ $SiO_2$ mass ratio of 0.56 at 1600 °C.

(2) During the interfacial reaction, Fe, Cr, Mg, and Al undergo redox interactions at the $FeCr_2O_4$/slag interface. MgO demonstrates superior diffusivity relative to $SiO_2$ and $Al_2O_3$, coupled with enhanced bonding affinity toward FeO and $Cr_2O_3$. This drives the predominant formation of $MgCr_2O_4$, $MgAl_2O_4$ and MgO-FeO solid solutions, which deposit on unreacted $FeCr_2O_4$ surfaces to form a boundary layer, thereby inhibiting slag-induced dissolution of $FeCr_2O_4$.

(3) The solubility of $FeCr_2O_4$ demonstrated a temperature-dependent enhancement, increasing from 0.081 wt% at 1500°C to 0.143 wt% at 1600°C. Kinetic analysis revealed that the surface dissolution reaction of $FeCr_2O_4$ particles constituted the rate-controlling step in the overall dissolution process. The activation energy of the dissolution reaction of $FeCr_2O_4$ in the $MgO\text{-}Al_2O_3\text{-}SiO_2$ slag is 65.43 kJ·mol$^{-1}$.

## Acknowledgments

*The authors are grateful for the financial support of this work from the National Natural Science Foundation of China (No. 52274406), China Baowu Low-Carbon Metallurgy Innovation Fund*

*(BWLCF202402), and the Fundamental Research Funds for the Central Universities (FRF-BD-23-02).*

### Author's Contributions

*Kang Shao: Writing- Original draft & Review & editing, Visualization, Data curation, Conceptualization. Zhang Chen: Formal analysis. Lijun Wang: Methodology, Supervision, Resources, Funding acquisition.*

### Conflict of Interest

*The authors declare that have no known competing financial interests or personal relationships that could have appeared to influence the work reported in this paper*

### Data Availability

*The raw/processed data required to reproduce the above findings cannot be shared at this time as the data also forms part of an ongoing study.*

### Reference

[1] P. Zhao, H. Zhang, J. Yu, H. Gao, Y. Cao, Y. Zhu, H. Zhao, Conditions for mutual conversion of Cr(III) and Cr(IV) in aluminum chromium slag, Journal of Alloys and Compounds, 788 (2019) 506-513. https://doi.org/10.1016/j.jallcom.2019.02.093

[2] S. Wu, S. Zhang, Y. Zhang, C. Gao, Reuse of vitrified argon oxygen decarburization slag as supplementary cementitious materials: Comprehensive performance and chromium immobilization mechanism, Construction and Building Materials, 348 (2022) 128647. https://doi.org/10.1016/j.conbuildmat.2022.128647

[3] S. Zhang, Y. Zhang, Z. Qu, Physicochemical property and chromium leaching behavior in different environments of glass ceramics prepared from AOD stainless steel slag, Journal of Alloys and Compounds, 805 (2019) 1106-1116. https://doi.org/10.1016/j.jallcom.2019.07.065

[4] P.K. Das, B.P. Das, P. Dash, Chromite mining pollution, environmental impact, toxicity and phytoremediation: a review, Environmental Chemistry Letters, 19 (2) (2021) 1369-1381. https://doi.org/10.1007/s10311-020-01102-w

[5] P. Jin, Z. Jiang, C. Bao, S. Hao, X. Zhang, The energy consumption and carbon emission of the integrated steel mill with oxygen blast furnace, Resources Conservation and Recycling, 117 (2017) 58-65. https://doi.org/10.1016/j.resconrec.2015.07.008

[6] Y. Yu, B. Li, Z. Fang, C. Wang, Energy and exergy analyses of pellet smelting systems of cleaner ferrochrome alloy with multi-energy supply, Journal of Cleaner Production, 285 (2021) 124893. https://doi.org/10.1016/j.jclepro.2020.124893

[7] P. Zhao, H. Zhang, J. Yu, H. Gao, Y. Cao, Y. Zhu, H. Zhao, Conditions for mutual conversion of Cr(III) and Cr(IV) in aluminum chromium slag, Journal of Alloys and Compounds, 788 (2019) 506-513. https://doi.org/10.1016/j.jallcom.2019.02.093

[8] F. Yuan, Z. Zhao, Y. Zhang, T. Wu, Effect of $Al_2O_3$ content on the viscosity and structure of CaO-$SiO_2$-$Cr_2O_3$- $Al_2O_3$ slags, International Journal of Minerals Metallurgy and Materials, 29 (8) (2022) 1522-1531. https://doi.org/10.1007/s12613-021-2306-2

[9] S. Wu, Y. Zhang, H. Li, S. Zhang, E. Kasai, C. Wang, Hydrogen-based pre-reduction of chromite: Reduction and consolidation mechanisms, International Journal of Hydrogen Energy, 50 (2024) 397-410. https://doi.org/10.1016/j.ijhydene.2023.09.026

[10] T. Gheno, D. Monceau, J. Zhang, D.J. Young, Carburisation of ferritic Fe-Cr alloys by low carbon activity gases, Corrosion Science, 53 (9) (2011) 2767-2777. https://doi.org/10.1016/j.corsci.2011.05.013

[11] C.M. Chang, Y.C. Chen, W. Wu, Microstructural and abrasive characteristics of high carbon Fe-Cr-C hardfacing alloy, Tribology International, 43 (5-6) (2010) 929-934. https://doi.org/10.1016/j.triboint.2009.12.045

[12] I. Kostitsyna, A. Shakhmatov, A. Davydov, Study of corrosion behavior of carbon and low-alloy steels in $CO_2$-containing environments; proceedings of the E3S Web of Conferences, F, 2019, EDP Sciences. https://doi.org/10.1051/e3sconf/201912104006

[13] S. Liu, X. He, Y. Wang, L. Wang, Cleaner and effective extraction and separation of iron from vanadium slag by carbothermic reduction-chlorination-molten salt electrolysis, Journal of Cleaner Production, 284 (2021) 124674. https://doi.org/10.1016/j.jclepro.2020.124674

[14] S. Liu, L. Wang, K.-C. Chou, Innovative method for minimization of waste containing Fe, Mn and Ti during comprehensive utilization of vanadium slag, Waste Management, 127 (2021) 179-188. https://doi.org/10.1016/j.wasman.2021.04.034

[15] F. Gu, Y. Zhang, Z. Su, Y. Tu, S. Liu, T. Jiang, Recovery of chromium from chromium-bearing slags produced in the stainless-steel smelting: A review, Journal of Cleaner Production, 296 (2021) 126467. https://doi.org/10.1016/j.jclepro.2021.126467

[16] O. Demir, R.H. Eric, Rate and mechanism of reduction-dissolution of chromite in liquid slags, High Temperature Materials and Processes, 32 (3) (2013) 255-263. https://doi.org/10.1515/htmp-2012-0133

[17] T. Wu, F. Yuan, Y. Zhang, Viscosity measurements of CaO-$SiO_2$-CrO slag, Isij International, 58 (2) (2018) 367-369. https://doi.org/10.2355/isijinternational.ISIJINT-2017-558

[18] L. Zhang, M. Chen, M. Huang, N. Wang, C. Wang, Dissolution kinetics of $SiO_2$ in FeO-$SiO_2$-$V_2O_3$-CaO-MnO-$Cr_2O_3$-$TiO_2$ system with different FeO contents, Metallurgical and Materials Transactions B-Process Metallurgy and Materials Processing Science, 52 (4) (2021) 2703-2714. https://doi.org/10.1007/s11663-021-02214-6

[19] Z. Wang, I. Sohn, Understanding the solidification and leaching behavior of synthesized Cr-containing stainless steel slags with varying $Al_2O_3/SiO_2$ mass ratios, Ceramics International, 47 (8) (2021) 10918-10926. https://doi.org/10.1016/j.ceramint.2020.12.211

[20] Y. Liu, M.-f. Jiang, L.-x. Xu, D.-y. Wang, A coupling dynamic model for dissolution and reduction of chromium ore in a smelting reduction converter,

Journal of Iron and Steel Research International, 19 (1) (2012) 5-10. https://doi.org/10.1016/S1006-706X(12)60039-9

[21] M.-f. Jiang, Y. Liu, D.-y. Wang, L.-x. Xu, Kinetic study on chromium ore dissolution in CaO-$SiO_2$-MgO-$Al_2O_3$ melts; Proceedings of the 137th Annual Meeting and Exhibition of the Minerals-Metals-and-Materials-Society, Mar 09-13, 2008, New Orleans, LA, 2008, 2008 Pages: 201.

[22] K. Morita, T. Shibuya, N. Sano, The solubility of the chromite in MgO-$Al_2O_3$-$SiO_2$-CaO melts at 1600° C in air, Tetsu-to-Hagané, 74 (4) (1988) 632-639. https://doi.org/10.2355/tetsutohagane1955.74.4_632

[23] H.G. Katayama, M. Satoh, M. Tokuda, Dissolution and reduction behaviors of chromite ore in molten slag, Tetsu-to-Hagané, 75 (10) (1989) 1883-1890. https://doi.org/10.2355/tetsutohagane1955.75.10_1883

[24] D. Yu, D. Paktunc, Kinetics and mechanisms of the carbothermic reduction of chromite in the presence of nickel, Journal of Thermal Analysis and Calorimetry, 132 (1) (2018) 143-154. https://doi.org/10.1007/s10973-017-6936-6

[25] D. Paktunc, J.P. Coumans, D. Carter, N. Zagrtdenov, D. Duguay, Mechanism of the direct reduction of chromite process as a clean ferrochrome technology, ACS engineering Au, 4 (1) (2024) 125-138. https://doi.org/10.1021/acsengineeringau.3c00057

[26] S. Yokoyama, M. Takeda, H. Oogusu, K. Ito, M. Kawakami, Effect of flux compositon on smelting reduction of chromite ore, Tetsu-to-Hagané, 78 (2) (1992) 215-222. https://doi.org/10.2355/tetsutohagane1955.78.2_215

[27] J. Blundy, E. Melekhova, L. Ziberna, M.C. Humphreys, V. Cerantola, R.A. Brooker, C.A. Mccammon, M. Pichavant, P. Ulmer, Effect of redox on Fe-Mg-Mn exchange between olivine and melt and an oxybarometer for basalts, Contributions to Mineralogy and Petrology, 175 (11) (2020) 103. https://doi.org/10.1007/s00410-020-01736-7

[28] Y. Bai, B.-X. Su, C. Chen, S.-H. Yang, Z. Liang, Y. Xiao, K.-Z. Qin, S.P. Malaviarachchi, Base metal mineral segregation and Fe-Mg exchange inducing extreme compositions of olivine and chromite from the Xiadong Alaskan-type complex in the southern part of the Central Asian Orogenic Belt, Ore Geology Reviews, 90 (2017) 184-192. https://doi.org/10.1016/j.oregeorev.2017.01.023

[29] K. Wei, L. Wang, S. Liu, X. He, Y. Xiao, K. Chou, Dissolution kinetics of synthetic $FeCr_2O_4$ in CaO–MgO–$Al_2O_3$–$SiO_2$ slag, Isij International, 62 (4) (2022) 617-625. https://doi.org/10.2355/isijinternational.ISIJINT-2021-497

[30] D.J. Andersen, D.H. Lindsley, P.M. Davidson, QUILF: A pascal program to assess equilibria among Fe-Mg-Mn-Ti oxides, pyroxenes, olivine, and quartz, Computers & Geosciences, 19 (9) (1993) 1333-1350. https://doi.org/10.1016/0098-3004(93)90033-2

# MEHANIZMI KINETIKE RASTVARANJA SPINELA $FeCr_2O_4$ U SISTEMU ŠLJAKE MgO–$Al_2O_3$–$SiO_2$: ELEMENTARNO RASTVARANJE I DIFUZIJA KOMPONENATA

**Kang Shao [a], Zhang Chen [a], Lijun Wang [a, b, *]**

[a] Univerzitet za nauku i tehnologiju u Pekingu, Kolaborativni inovacioni centar za tehnologiju čelika, Peking, Kina

[b] Univerzitet za nauku i tehnologiju u Pekingu, Ključna državna laboratorija za naprednu metalurgiju, Peking, Kina

***Apstrakt***

*Proces direktnog legiranja redukcijom rastopljenog hromita predstavlja ključnu metaluršku tehnologiju u proizvodnji nerđajućeg čelika, nudeći prednosti kao što su smanjena potrošnja ugljenika i poboljšana efikasnost proizvodnje. U ovoj studiji, kako bi se otkrio mehanizam rastvaranja hromita, korišćena je čista faza sintetičkog $FeCr_2O_4$, glavne komponente hromita, da zameni hromit sa kompleksnim sastavom. Kinetika rastvaranja $FeCr_2O_4$ u MgO-$Al_2O_3$-$SiO_2$ šljaci sistematski je ispitana kao funkcija intenziteta mešanja, odnosa MgO/$SiO_2$ i temperature, otkrivajući njegove neizotermne karakteristike reaktivnog rastvaranja. Eksperimentalni rezultati su pokazali da rastvorljivost $Cr_2O_3$ pokazuje trend početnog povećanja praćenog naknadnim smanjenjem kako se maseni odnos MgO/$SiO_2$ povećava. Maksimalna rastvorljivost je uočena pri masenom odnosu MgO/$SiO_2$ od 0,56. Dodatno, studije povezane sa temperaturom su pokazale da se rastvaranje $FeCr_2O_4$ progresivno povećava sa porastom temperature pri povišenim termičkim uslovima (1500-1600 °C). U međuvremenu, analize skenirajuće elektronske mikroskopije (SEM) su potvrdile da međufazna reakcija između $FeCr_2O_4$ i komponenti šljake generiše $MgAl_2O_4$, $MgCr_2O_4$ i MgO-xFeO čvrst rastvor, formirajući granični sloj na površini nereagovale faze $FeCr_2O_4$. Reakcija rastvaranja na površini $FeCr_2O_4$ predstavljala je korak koji kontroliše brzinu u procesu rastvaranja. Izračunata aktivaciona energija procesa rastvaranja iznosila je 65,43 kJ·mol$^{-1}$.*

***Ključne reči:*** *Šljaka; Rastvaranje; MgO/$SiO_2$; Međufaza; Kinetika rastvaranja*